THE JOURNAL OF PHYSICAL CHEMISTRY C

Article

Cite This: J. Phys. Chem. C 2019, 123, 2202−2215

pubs.acs.org/JPCC

Computational Study of Short-Pulse Laser-Induced Generation of Crystal Defects in Ni-Based Single-Phase Binary Solid−Solution Alloys

Miao He,[†] Chengping Wu,[†] Maxim V. Shugaev,[†] German D. Samolyuk,[‡] and Leonid V. Zhigilei*[,†]

[†]Department of Materials Science and Engineering, University of Virginia, 395 McCormick Road, Charlottesville, Virginia 22904-4745, United States

[‡]Materials Science and Technology Division, Oak Ridge National Laboratory, Oak Ridge, Tennessee 37831, United States

Supporting Information

ABSTRACT: Single-phase concentrated solid−solution alloys exhibit enhanced mechanical characteristics and radiation damage resistance, making them promising candidate materials for applications involving an exposure to rapid localized energy deposition. In this paper, we use large-scale atomistic modeling to investigate the mechanisms of the generation of vacancies, dislocations, stacking faults, and twin boundaries in Ni, $Ni_{50}Fe_{50}$, $Ni_{80}Fe_{20}$, and $Ni_{80}Cr_{20}$ targets irradiated by short laser pulses in the regime of melting and resolidification. The decrease in the thermal conductivity and strengthening of the electron−phonon coupling due to the intrinsic chemical disorder in the solid-solution alloys are found to have important implications on localization of the energy deposition and generation of thermoelastic stresses. The interaction of the laser-induced stress waves with the melting front is found to play a key role in roughening of the crystal−liquid interface and generation of dislocations upon the solidification. A common feature revealed in the structural analysis of all irradiated targets is the presence of high vacancy concentrations exceeding the equilibrium values at the melting temperature by about an order of magnitude. On the basis of the results of molecular dynamics simulations of solidification occurring at fixed levels of undercooling, the generation of vacancies is correlated with the velocity of the solidification front, and the processes responsible for creating the strong vacancy supersaturation are revealed. The suppression of the vacancy generation in the solid−solution alloys is also revealed and related to combined effect of enhanced vacancy mobility and higher energy of the vacancy formation in the alloy systems. The analysis of the first atomic shells surrounding the vacancy sites in Ni−Fe alloys uncovers the preference for the vacancy sites to be surrounded by Fe atoms and suggests that atomic-scale chemical heterogeneities may play an important role in defining the behavior and properties of the single-phase concentrated solid-solution alloys.

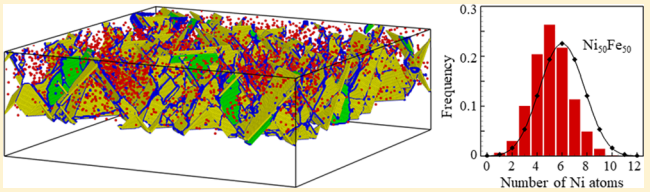

1. INTRODUCTION

Short-pulse laser irradiation of a metal target provides unique opportunities for investigation of material behavior under conditions of strong electronic, thermal, phase, and mechanical nonequilibrium, and can lead to the generation of unusual phases and microstructure (arrangement of crystal defects) in a surface region of the irradiated target.[1−14] In particular, in the regime of laser melting and resolidification, the shallow melt depths produced by the highly localized energy deposition and the high thermal conductivity of metals can result in extreme cooling rates, deep undercooling, and rapid resolidification.[7,8,11−19] Highly nonequilibrium densities and configurations of crystal defects in this case can be produced through the generation of various defects at the rapidly advancing solidification front,[7,9,14,20,21] emission of dislocations due to the dynamic relaxation of laser-induced thermoelastic stresses,[2−6,20,21] and thermally activated rearrangements of the defect configurations during the short thermal spike that follows the laser excitation.

The laser-induced generation of crystal defects has important implications for the modification of mechanical, optical, and chemical properties of the surface. The accumulation of subsurface defects has also been discussed as one of the possible mechanisms responsible for incubation effect observed in multipulse irradiation of metal targets, when the laser fluence threshold for ablation/damage decreases with increasing number of laser pulses applied to the same area.[9,22−27] Because of the relatively shallow depth of the laser-modified zone and the ultrafast rates of processes induced by short pulse laser irradiation, the direct time-resolved experimental probing of the generation and evolution of the defect configurations, however, still remains out of reach even for the most advanced pump−probe techniques.[19,28−31] The confinement of the laser-induced structural modifications within a relatively thin surface region of the target also

Received: October 11, 2018
Revised: December 6, 2018
Published: January 4, 2019

DOI: 10.1021/acs.jpcc.8b09922
J. Phys. Chem. C 2019, 123, 2202−2215

presents a challenge for *ex situ* characterization, although a number of electron backscatter diffraction studies revealing the presence of high densities of dislocations[2−6] and twin boundaries[1,7] in laser-processed metal targets have recently been reported.

A reliable physical interpretation of the experimental evidence of the laser-induced generation of crystal defects in terms of the rapid laser-induced structural transformations can be provided by large-scale atomistic modeling. Indeed, the ability of atomistic simulations to provide insights into the mechanisms responsible for surface nanocrystallization,[8,11−13] growth twinning,[7] emission of dislocations,[14,20,21] and strong vacancy supersaturation[9,20,21] has been demonstrated in modeling of laser interactions with one-component Cr, Ag, and Ni targets.

In the study reported in this paper, we extend atomistic modeling to binary Ni-based solid−solution alloys and focus our attention on evaluation of the effect of chemical disorder on the generation and evolution of crystal defects in targets undergoing rapid melting and resolidification. The composition of three binary alloys used in this study, $Ni_{50}Fe_{50}$, $Ni_{80}Fe_{20}$, and $Ni_{80}Cr_{20}$, is selected to ensure that the alloys remain in the chemically disordered state under regular cooling conditions.[32,33] The binary single-phase solid−solution alloys can, therefore, serve as model systems for investigation of the implications of chemical disorder on the behavior and properties of an emerging class of multicomponent solid−solution alloys that exhibit enhanced mechanical characteristics[34] and radiation damage resistance,[35] making them promising candidate materials for nuclear energy applications. For Ni-based solid−solution alloys, in particular, the site-to-site random variation of local chemical environments and corresponding lattice distortions have been shown to result in the suppression, as compared to pure Ni, of damage accumulation under high-energy particle irradiation.[35−40]

Although the atomistic simulations of the displacement cascades generated by high-energy particle bombardment have provided important information on the sensitivity of the defect generation to the alloy composition,[37−39] the relatively small sizes of the individual collision cascades and rapid quenching in the regions of the energy deposition make it difficult to establish direct links between the characteristics of radiational damage, energetics and mobility of individual defects, and the evolution of thermodynamic conditions in the irradiated material. In contrast, the laser irradiation can create energy densities comparable to those in the high-energy ion tracks in much larger regions of the irradiated targets, thus providing more reliable statistical information on the structural response of the material to the strong excitation. Moreover, the thermodynamic parameters and structural transformations are evolving slower and in a more regular manner in laser−material interaction as compared to those in the high-energy particle bombardment, thus enabling more detailed analysis of the connections between the rapidly changing thermodynamic conditions, nonequilibrium phase transformations, and the generation of crystal defects.

The computational model developed for atomistic simulations of laser interactions with metals and its parameterization for Ni−Fe and Ni−Cr single-phase solid−solution alloys are briefly described next, in Section 2. The results of atomistic simulations of the generation of crystal defects by laser-induced melting and resolidification of Ni, $Ni_{50}Fe_{50}$, $Ni_{80}Fe_{20}$, and $Ni_{80}Cr_{20}$ targets are reported in Section 3. The mechanisms of the vacancy generation and the reasons for reduced vacancy concentrations generated in the alloy targets are discussed in Section 4 based on the results of simulations of solidification performed under conditions of constant pressure and temperature. The computational predictions on the generation of crystal defects in the solid−solution alloys are summarized in Section 5.

2. COMPUTATIONAL MODEL

The simulations of laser melting and resolidification of Ni and Ni-based alloy targets reported in this paper are performed with a computational model combining the classical atomistic molecular dynamics (MD) method with the continuum-level two-temperature model (TTM).[41,42] In the original TTM,[43] the evolution of the lattice and electron temperatures in the irradiated target is described by two coupled nonlinear differential equations that account for the laser excitation of conduction-band electrons, energy exchange between the electrons and atomic vibrations due to the electron−phonon coupling, and the electron heat transfer. In the combined TTM−MD method, the MD substitutes the TTM equation for the lattice temperature in the surface region of the target, where laser-induced structural and phase transformations take place. The diffusion equation for the electron temperature is solved by a finite difference method simultaneously with MD integration of the equations of atomic motion. The cells in a three-dimensional finite difference discretization are mapped to the corresponding volumes of the MD system,[11,12,14,42] and the local lattice temperature is defined for each cell from the average kinetic energy of thermal motion of atoms. The atoms crossing cell boundaries carry the corresponding electron thermal energy along, thus ensuring the total energy conservation.[44] The electron temperature enters a coupling term added to the MD equations of motion to account for the energy exchange between the electrons and the lattice.[41] A complete description of the TTM−MD model is provided elsewhere,[41,42] and below we only outline the computational setup and provide parameters used in the simulations reported in this paper.

The temperature dependences of the thermophysical material properties included in the TTM equation for the electron temperature (electron−phonon coupling factor, electron heat capacity and thermal conductivity) are taken in the forms that account for the thermal excitation from the electron states below the Fermi level[45−47] and are provided in Supporting Information. The interatomic interactions in the MD part of the TTM−MD model are described by the embedded atom method (EAM) potential developed for the Ni−Fe−Cr system by Bonny *et al.*[48] Some of the material properties predicted by this potential, such as elastic constants, lattice parameters, vacancy formation and migration energies, are evaluated in ref 48 and are found to agree reasonably well with experimental data and predictions of density functional theory calculations. The melting temperatures of Ni, $Ni_{50}Fe_{50}$, $Ni_{80}Fe_{20}$, and $Ni_{80}Cr_{20}$, as well as the temperature dependencies of the lattice heat capacity in the solid state and surface tension in the molten state are calculated for the Bonny EAM potential in this work and are summarized in the Supporting Information.

The depth of the surface parts of the targets represented with atomistic resolution is 70 nm in all simulations, and the initial MD systems have the face-centered cubic (fcc) crystal structure and (001) orientation of the free surface. In the

DOI: 10.1021/acs.jpcc.8b09922
J. Phys. Chem. C 2019, 123, 2202−2215

Table 1. Distinct Physical Regimes of the Response of Ni and Ni-Based Solid−Solution Alloy Targets to the Irradiation by 50 fs Laser Pulses at F_{abs} Ranging from 200 to 600 J/m^2 Predicted in Small-Scale TTM−MD Simulations

Fluence (J/m^2)	200	300	400	500	600
Ni	No melting	No melting	No melting	Melting and resolidification	Subsurface cavitation
$Ni_{50}Fe_{50}$	No melting	Melting and resolidification	Subsurface cavitation	Spallation	Spallation
$Ni_{80}Fe_{20}$	No melting	Melting and resolidification	Spallation	Spallation	Spallation
$Ni_{80}Cr_{20}$	No melting	Melting and resolidification	Spallation	Spallation	Spallation

solid−solution Ni-based alloys, the Fe and Cr atoms occupy randomly selected lattice sites. The dimensions of the computational systems in the lateral directions are 7 nm × 7 nm in the small-scale simulations (320 thousand atoms) discussed in Section 3.1 and aimed at establishing the threshold fluences delineating transitions between different regimes of the material response to the laser irradiation. Once the fluence regimes are established, one large-scale TTM−MD simulation is performed for each target composition under irradiation conditions leading to a transient melting and resolidification of a ∼20 nm deep region of the target. These simulations, discussed in Sections 3.2 and 3.3, are aimed at providing microscopic information of the laser-induced generation of crystal defects and are performed with the lateral size of the computational systems increased to 100 nm × 100 nm, which corresponds to about 65 million atoms in the MD part of the computational domain.

The periodic boundary conditions are applied in the lateral directions, parallel to the surface of a target, and a dynamic pressure-transmitting boundary condition[49,50] is applied at the bottom of the MD part of the computational domain to mimic the nonreflective propagation of the laser-induced pressure waves into the bulk of the target. In the deeper part of the target, below the bottom boundary of the MD region, the conventional TTM equations for the lattice and electron temperatures are solved on a grid extending down to the depth of 2 μm, which ensures a negligible change in the electron and lattice temperatures at the bottom of the computational domain on the simulated timescales. Before applying laser irradiation, all TTM−MD systems are equilibrated at 300 K.

The laser irradiation of the target is represented through a source term added to the TTM equation for the electron temperature.[41] The source term describes excitation of the conduction band electrons by a laser pulse with a Gaussian temporal profile and reproduces the exponential attenuation of laser intensity with the depth under the surface. In all simulations, the optical absorption depth is approximated as 14.5 nm, taken based on the value of absorption coefficient of pure Ni at a laser wavelength of 800 nm.[51] The laser pulse durations, τ_L, defined as full width at half maximum of the Gaussian profile, is 50 fs in all small-scale simulations and either 100 fs or 50 ps in the large-scale simulations. The reflectivity of the surface is not defined in the model because the absorbed laser fluence, F_{abs}, rather than the incident fluence is used in the presentation of the simulation results. The small-scale simulations are performed at F_{abs} ranging from 200 to 600 J/m^2, while the irradiation conditions (τ_L and F_{abs}) in the large-scale simulations are chosen to ensure that the simulations are in the melting and resolidification regime.

The interpretation of the densities and types of laser-induced crystal defects predicted in TTM−MD simulations is assisted by a series of additional MD simulations where the defects are generated in the course of a rapid solidification of Ni and Ni-based alloys proceeding under well-controlled pressure and temperature conditions. These additional simulations are performed for crystal−liquid coexistence systems with dimensions of 7 nm × 7 nm × 300 nm (1.28 million atoms) created by combining two 120 nm long liquid parts with a 60 nm-long fcc crystal into a single system. Periodic boundary conditions are then applied in all three directions, forming a system where a solid slab is surrounded by molten material. The fcc crystal is oriented so that its [001] direction is aligned with the longest axis of the combined system. The parts of the combined system are pre-equilibrated at a desired temperature and zero pressure. The liquid subsystem is prepared in a constant zero pressure simulation, where a crystal is first heated above the limit of its thermodynamic stability against the onset of homogeneous melting, ∼1.2−1.3 T_m,[52−54] leading to the rapid melting of the whole system. The molten material is then cooled down to the desired temperature, below T_m. The undercooled liquid remains in the metastable state because of the absence of any nucleation sites and relatively slow rate of homogeneous nucleation of new crystallites at moderate levels of undercooling. After the combined systems are prepared, the solidification simulations are performed at zero pressure and a range of temperatures covering those observed in the TTM−MD simulations. The crystal−liquid coexistence systems are subdivided into ∼4 nm thick slices along the [001] direction, and the temperature is controlled through the Berendsen thermostat algorithm[55] applied to the individual slices. This slice-by-slice temperature control eliminates the appearance of temperature spikes near the advancing solidification fronts due to the release of the latent heat of melting and enables simulation of the solidification at a well-controlled temperature of the crystal−liquid interface. In both the preparation of the

DOI: 10.1021/acs.jpcc.8b09922
J. Phys. Chem. C 2019, 123, 2202−2215

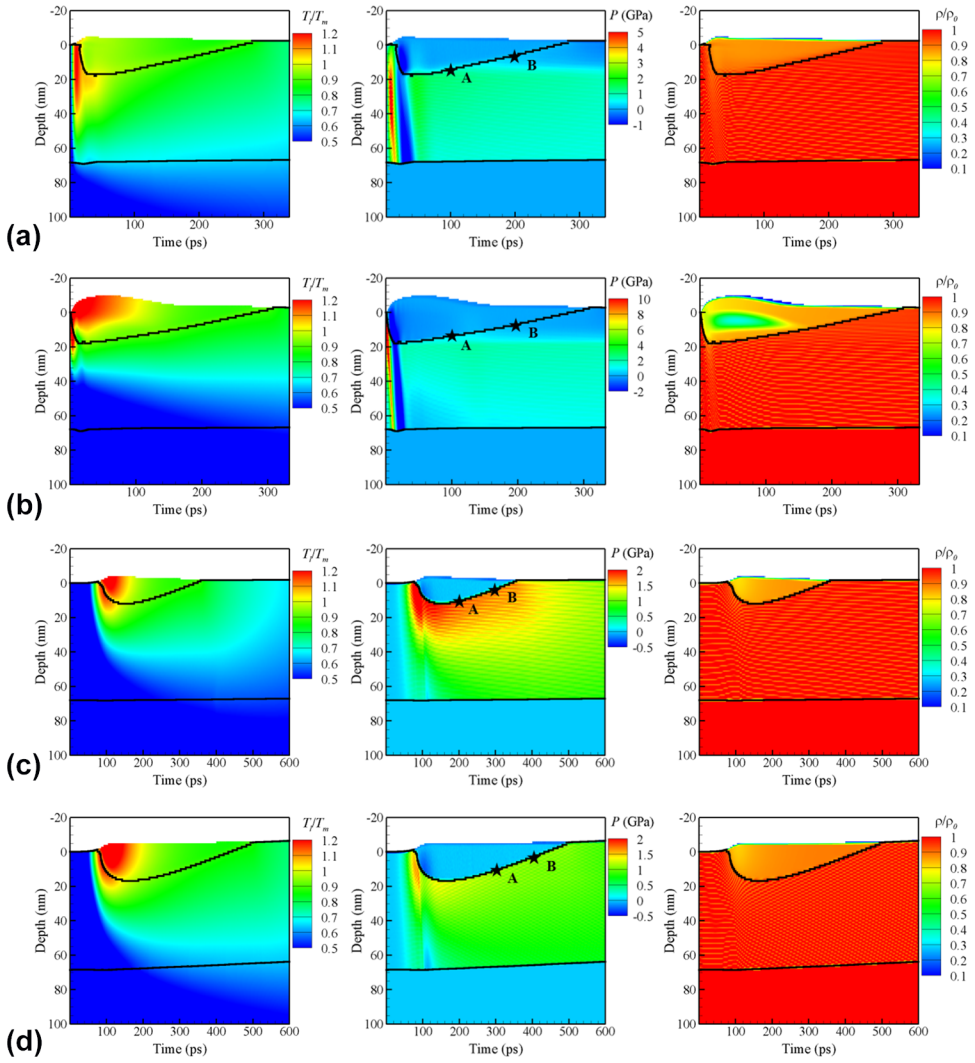

Figure 1. Contour plots of the spatial and temporal evolution of lattice temperature, pressure, and density in the surface regions of Ni (a), $Ni_{50}Fe_{50}$ (b), $Ni_{80}Fe_{20}$ (c), and $Ni_{80}Cr_{20}$ (d) targets irradiated in the regime of melting and resolidification. The temperature scale is normalized by the equilibrium melting temperature, T_m, which is different for each target material and is given in the Supporting Information. The black solid lines near the surfaces of the targets show the movement of the crystal–liquid interface, and the black lines in the lower parts of the contour plots show the location of the nonreflecting boundary applied at the bottom of the MD part of the computational domain. The black stars marked by letters "A" and "B" show the moments of time for which interface roughness is evaluated and provided in Table 2. The irradiation conditions are τ_L = 100 fs and F_{abs} = 500 J/m^2 for Ni (a), τ_L = 100 fs and F_{abs} = 400 J/m^2 for $Ni_{50}Fe_{50}$ (b), and τ_L = 50 ps and F_{abs} = 400 J/m^2 for $Ni_{80}Fe_{20}$ and $Ni_{80}Cr_{20}$ (c,d). Snapshots of atomic configurations generated in the simulations are shown in Figure 2.

liquid part of the system and the solidification simulations, the pressure control is done through the Berendsen barostat algorithm[55] applied along the z-axis of the system only, with sizes of the systems along the x and y directions fixed at values that correspond to a crystal equilibrated at zero pressure at the desired temperature. This enables combination of the liquid and crystalline parts of the system at the sample preparation stage and eliminates the appearance of anisotropic lattice distortions in the simulations of solidification. The solidification velocities are then calculated by tracking the movement of the two crystal–liquid interfaces, and the defects generated in the parts of the system where the solidification takes place in the steady-state regime (constant velocity of the solidification front) are analyzed.

3. GENERATION OF CRYSTAL DEFECTS BY LASER-INDUCED MELTING AND RESOLIDIFICATION

3.1. Fluence Thresholds for Melting and Spallation.

The main goal of this study is to investigate the effect of the chemical disorder on the generation of crystal defects under condition of rapid laser-induced melting and resolidification. To enable direct comparison between the results obtained for pure Ni and Ni-based solid–solution alloys, we first choose the irradiation conditions that produce transient melting and resolidification of about 20 nm deep regions in targets of all compositions considered in this work. The selection of the irradiation conditions is based on the results of four series of computationally-inexpensive small-scale simulations performed for each material and aimed at establishing the threshold fluences delineating transitions between different regimes of the material response to the laser irradiation, namely, melting

DOI: 10.1021/acs.jpcc.8b09922
J. Phys. Chem. C 2019, 123, 2202–2215

and resolidification, subsurface cavitation, and spallation. The regimes identified in these simulations, performed for different target compositions and a broad range of laser fluences, are summarized in Table 1.

The material response to laser irradiation identified in the simulations is following the sequence of the regimes established in earlier computational studies, for example, refs 12, 16, and 42 For pure Ni, the threshold for surface melting is found to be between 400 and 500 J/m^2, which is consistent with the melting threshold identified in simulations[7] performed with Mishin EAM potential[56] but higher than the melting threshold of 360 J/m^2 reported in ref 16 for Johnson EAM Ni,[57] which significantly underestimates the melting temperature of Ni.[16] As the fluence increases to 600 J/m^2, the relaxation of the laser-induced stresses generated in the surface region of the Ni target under conditions of stress confinement[58,59] results in the transient appearance and collapse of voids in a subsurface region of the target. Further increase of the laser fluence leads to the coalescence of voids and ejection of a top liquid layer in the process commonly called spallation.[11,16,42] The fluence thresholds for surface melting and spallation predicted in the simulations are much closer to each other than those in earlier simulations reported for Ni.[7,16] The early onset of void nucleation and spallation can be related to the substantial underestimation, with respect to experimental values, of the surface tension by the Bonny EAM potential, see the Supporting Information. The low surface tension reduces the energy cost for the subsurface cavitation and spallation, thus narrowing the range of fluences where the effect of the laser irradiation is limited to the melting and resolidification. This range of fluences, however, is still sufficient for investigation of the generation of crystal defects at the solidification front investigated in the present study.

As discussed in the Supporting Information, the intrinsic chemical disorder in the Ni-based alloys causes stronger electron−phonon coupling and lower thermal conductivity as compared to pure Ni, leading to faster electron−phonon equilibration and more localized heating of the surface region of the target. As a result, the melting threshold is significantly reduced for all Ni-based alloys, down to 200−300 J/m^2 as compared to 400−500 J/m^2 for pure Ni. Moreover, the faster and more localized lattice heating in the alloys results in the buildup of stronger compressive stresses and unloading tensile waves, causing the appearance of subsurface voids (cavitation) and onset of spallation at lower fluences. In the simulations performed at 400 J/m^2, the subsurface cavitation is followed by the collapse of the voids in $Ni_{50}Fe_{50}$ target, while in $Ni_{80}Fe_{20}$ and $Ni_{80}Cr_{20}$ targets the voids grow, coalesce, and percolate, leading to the spallation of a liquid layer. This difference can be explained by the noticeably higher surface tension in $Ni_{50}Fe_{50}$ as compared to the other two alloys, see Figure S3a in the Supporting Information.

In this paper, the goal is to investigate the generation of crystal defects in the course of laser-induced melting and resolidification. Therefore, the irradiation conditions for the large-scale simulations discussed below are chosen to avoid spallation and to ensure similar maximum melting depth in targets of all four compositions. For Ni and $Ni_{50}Fe_{50}$ targets, the pulse duration of 100 fs is used, and the absorbed fluences of 500 J/m^2 and 400 J/m^2 are chosen, respectively, to melt surface regions down to similar maximum depths while staying below the spallation thresholds. The transient appearance and collapse of voids in $Ni_{50}Fe_{50}$ at 400 J/m^2 takes place in the molten region before the arrival of the solidification front and does not affect the generation of crystal defects. For $Ni_{80}Fe_{20}$ and $Ni_{80}Cr_{20}$ alloy targets irradiated with 50 or 100 fs laser pulses, the spallation occurs before the desired melting depth is reached. Therefore, the large-scale simulations for these two targets are performed with longer 50 ps laser pulses at an absorbed fluence of 400 J/m^2, which produces melting depth similar to that in the other two simulations. The longer pulse duration allows for a partial relaxation of the thermoelastic stresses during the laser heating, significantly reduces the strength of the unloading tensile wave, and prevents spallation.

3.2. Large-Scale Simulations of Melting and Resolidification. Four large-scale simulations are performed for Ni, $Ni_{50}Fe_{50}$, $Ni_{80}Fe_{20}$, and $Ni_{80}Cr_{20}$ targets irradiated in the regime of melting and resolidification, and the corresponding spatial and temporal evolution of lattice temperature, pressure, and density is shown in Figure 1. Laser excitation of conduction band electrons followed by the electron−phonon equilibration leads to the temperature increase in the surface regions of the irradiated targets. As discussed above, in Section 3.1, the stronger electron−phonon coupling in the alloys leads to the confinement of the initial lattice heating in much shallower surface regions of the targets, as can be seen from the temperature contour plots. This stronger confinement of the initial energy deposition explains why substantially lower laser fluences are required for producing melting depth in the alloy targets similar to that in Ni.

The temperature of the lattice in the surface region quickly exceeds the melting temperatures of the target materials, leading to rapid melting of the surface regions of the irradiated targets. For targets irradiated by 100 fs laser pulses, the surface is heated up to 1.2 T_m by 10 ps in Ni and by 1.2 ps in $Ni_{50}Fe_{50}$, again reflecting the stronger electron−phonon coupling in the alloy. As soon as this critical level of superheating is reached, rapid homogeneous melting of about 18 nm deep surface layers takes place in both targets. For $Ni_{80}Fe_{20}$ and $Ni_{80}Cr_{20}$, the heating is slower and is controlled by the rate of the laser energy deposition rather than the electron−phonon coupling (τ_L = 50 ps is more than 10 times longer than the characteristic time of electron−phonon equilibration, τ_{e-ph}). As a result, the melting starts from the surface when the surface temperature exceeds T_m at ∼75 ps, that is, around the time when the intensity of the Gaussian laser pulse reaches its maximum, and the melting front accelerates as more energy is deposited during the second half of the laser pulse. Because of the kinetic constraints on the melting front propagation,[60] the crystal lattice below the molten material is superheated up to 1.17−1.19 T_m before the arrival of the melting front, which propagates to the maximum depth of 12 nm and 17 nm in the $Ni_{80}Fe_{20}$ and $Ni_{80}Cr_{20}$ targets, respectively.

The local temperature at the crystal−liquid interface drops below T_m, and the melting turns into solidification at ∼50 ps after the start of the simulation for Ni, at ∼20 ps for $Ni_{50}Fe_{50}$, at ∼150 ps for $Ni_{80}Fe_{20}$, and at ∼165 ps for $Ni_{80}Cr_{20}$. The solidification velocity increases up to the maximum levels of 70−90 m/s as the temperature of the interface decreases down to the maximum undercooling of ∼0.9 T_m reached by the end of the resolidification process in all simulations. As can be seen from the temperature contour plots, the release of the latent heat of melting increases the local temperature at the solidification front and reduces the level of undercooling with respect to the maximum one reached at the molten surface, ∼0.85−0.87 T_m. Overall, as can be seen from the

DOI: 10.1021/acs.jpcc.8b09922
J. Phys. Chem. C 2019, 123, 2202−2215

temperature contour plots and the black lines showing the progression of the crystal−liquid interfaces, the heating, melting, cooling, and epitaxial resolidification proceed in a qualitatively similar manner in all four simulations.

In the simulations performed with τ_L = 100 fs, $\tau_L < \tau_{e-ph}$, and the time of the lattice heating is defined not by τ_L but by the time of the energy transfer from the hot electrons to the lattice, that is, by τ_{e-ph}. For both pure Ni and $Ni_{50}Fe_{50}$, τ_{e-ph} is shorter than the time needed for the mechanical relaxation (expansion) of the heated volume, leading to the generation of strong compressive stresses in the surface regions of the targets, as can be seen from the pressure plots in Figure 1a,b. In each of the two simulations, the relaxation of the compressive stresses drives the strong compressive pressure wave deeper into the bulk of the target and induces an unloading tensile wave that follows the compressive component. The compressive and tensile components of the pressure wave propagate without any noticeable reflection from the boundary separating the MD and continuum parts of the model. After the laser-induced pressure wave leaves the surface area of the target, zero pressure establishes in the molten region, while the residual thermoelastic stresses, which cannot relax by uniaxial expansion of the crystal lattice in the direction normal to the surface, remain in crystalline part of the target.[16] These quasi-static compressive stresses, however, are relaxed in the top parts of the resolidified regions of the targets due to the generation of high density of crystal defects, as discussed in the next section.

Interestingly, the magnitudes of the compressive and tensile components of the stress wave generated in the $Ni_{50}Fe_{50}$ target are substantially higher than those in the pure Ni target, even though the absorbed fluence of 400 J/m^2 applied to the alloy target is 20% lower than that used in the simulation of pure Ni target. This observation can be related to the stronger electron−phonon coupling in the alloy (see Figure S1b in the Supporting Information), leading to a shorter τ_{e-ph} and a more abrupt heating of the lattice. The increased magnitude of the tensile unloading wave is sufficient for inducing cavitation in the molten part of the target, which is apparent in the density plot shown in Figure 1b and proceeds through the nucleation and growth of subsurface voids. At a sufficiently high fluence, above the spallation threshold, the cavitation process can lead to the ejection of a liquid layer from the target, for example, refs 12, 16, 42, and 58. The voids can also be captured by the solidification front,[11] leading to the "swelling" of the surface region and formation of frozen subsurface nanovoids observed in experiments, for example, refs 11, 61, and 62. In the simulation illustrated by Figure 1b, however, the voids collapse because of the surface tension prior to the arrival of the solidification front and do not affect the microstructure of the resolidified region. Note that the cavitation occurs in $Ni_{50}Fe_{50}$ alloy and not in pure Ni despite the lower surface tension of the latter (see Figure S3a in Supporting Information), which is expected to facilitate the cavitation and spallation. This observation highlights the dominant role of the increased electron−phonon coupling and stronger stress confinement in defining the conditions for the generation of subsurface voids.

In the simulations performed for $Ni_{80}Fe_{20}$ and $Ni_{80}Cr_{20}$ alloys with longer τ_L = 50 ps, $\tau_L > \tau_{e-ph}$, and the time of the lattice heating is defined by τ_L rather than τ_{e-ph}. Thus, despite the strong electron−phonon coupling in the alloys, the condition for the stress confinement is not realized, and the thermoelastic stresses associated with the laser heating are largely relaxed during the laser energy deposition, as can be seen from much lower levels of pressure in Figure 1c,d as compared to those in Figure 1a,b. No subsurface voids are generated in these simulations, and the response to the laser irradiation is limited to melting and resolidification of surface regions of the targets.

3.3. Generation of Crystal Defects. The visual picture of the laser-induced melting and resolidification discussed in the previous section is provided by four series of snapshots of the top 30 nm deep surface layers of the Ni, $Ni_{50}Fe_{50}$, $Ni_{80}Fe_{20}$, and $Ni_{80}Cr_{20}$ targets shown in Figure 2. The local structural environment is determined for each atom with a structure identification method developed in refs 63−65, all atoms with local fcc structure are blanked, and only the molten regions and crystal defects are shown in Figure 2. The transient appearance of the molten surface regions shown by blue color in Figure 2 is consistent with the discussion of the melting and resolidification processes based on the contour plots provided in the previous section. The microstructures of the resolidified surface regions in Ni and $Ni_{50}Fe_{50}$ targets irradiated by 100 fs laser pulses feature higher density of vacancies, dislocations, stacking faults, and twin boundaries, with the latter two types of defects being particularly abundant in the $Ni_{50}Fe_{50}$ target. In contrast, the defects produced in $Ni_{80}Fe_{20}$ and $Ni_{80}Cr_{20}$ targets irradiated by longer 50 ps laser pulses are largely limited to vacancies and vacancy clusters, with only a few small dislocation loops observed in the $Ni_{80}Cr_{20}$ target. The mechanisms of the generation of crystal defects in the course of the laser-induced melting and resolidification are discussed next for each of the target materials.

Before discussing the very high vacancy concentrations generated in all four simulations, let us first consider the mechanisms of the generation of dislocations, stacking faults and twin boundaries, which are found to be sensitive to both the target composition and irradiation conditions. Starting from the simulation performed for the pure Ni target, the formation of several twin boundaries (green) and stacking faults (yellow) outlined by Shockley partial dislocations can be seen in the last snapshot in Figure 2a and an enlarged top view of the final configuration shown in Figure 3a. The generation of the partial dislocations can be related to the roughness of the crystal−liquid interface formed by the end of the rapid melting process. The unloading tensile wave, produced due to the dynamic relaxation of the laser-induced stresses, passes through the melting front at ∼20 ps, Figure 1a, reduces the crystal stability against melting,[53] and facilitates the homogeneous nucleation of liquid regions in the superheated crystal, Figure 2a. As a result, the molten layer formed by 50 ps is separated from the crystalline bulk of the target by a mushy zone where nanoscale crystalline and molten region are mixed. The following solidification process starts from a rough interface and results in the formation of Frank partial dislocations upon folding of deep troughs that produces areas with missing atomic planes incorporated into the growing crystal. Frank partials split into various combinations of stair rod and Shockley partials connected to the solidification front and extending in the course of solidification. In addition to the dislocations, the formation of growth twins is activated on several (111) facets of the rough solidification front advancing in (001) direction when the temperature at the front drops below the critical level required for the onset of growth twining.[7]

DOI: 10.1021/acs.jpcc.8b09922
J. Phys. Chem. C 2019, 123, 2202−2215

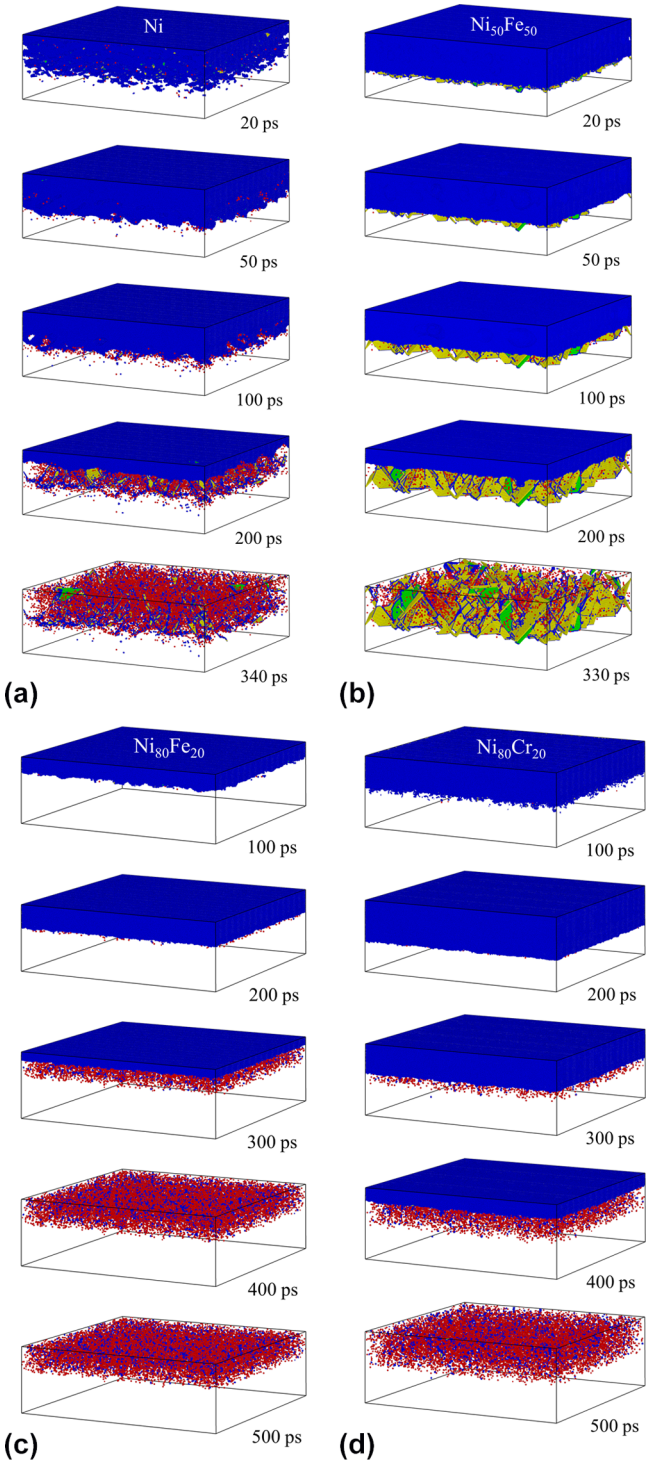

Figure 2. Snapshots of the surface regions of Ni (a), $Ni_{50}Fe_{50}$ (b), $Ni_{80}Fe_{20}$ (c), and $Ni_{80}Cr_{20}$ (d) targets irradiated in the regime of melting and resolidification. Only the top 30 nm thick surface regions of the irradiated targets are shown in the snapshots. The atoms with local fcc structure are blanked to expose the defect structures. The remaining atoms are colored by their local structural environment so that blue color corresponds to atoms that belong to the liquid phase or make up dislocation cores, atoms surrounding vacancies are colored red, stacking faults are colored yellow, and twin boundaries are colored green.

The defect configuration generated in the $Ni_{50}Fe_{50}$ target is visually very different from the one discussed above for pure Ni

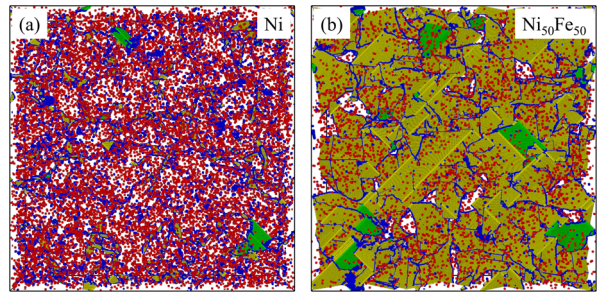

Figure 3. Top view of the crystal defects generated in the surface regions of Ni (a) and $Ni_{50}Fe_{50}$ (b) targets by the laser-induced melting and resolidification. The snapshots are shown for times of 340 and 330 ps after the laser irradiation of Ni and $Ni_{50}Fe_{50}$, respectively. All atoms with the fcc local crystal structure are blanked and the same coloring scheme as in Figure 2 is used.

and features a high density of stacking faults, Figures 2b and 3b. The formation of the stacking faults can be related to the emission of numerous partial dislocations from the crystal–liquid interface at the end of melting process, when strong tensile wave passes through the interface, Figure 1b. As discussed in Section 3.2, the higher strength of the electron–phonon coupling in the alloy as compared to pure Ni is responsible for the generation of stronger stress wave, which, in turn, generates the resolved shear stresses that are sufficient for the dislocation emission. The Shockley partial dislocations emitted from the melting front leave behind stacking faults that can be seen as earlier as 20 ps after the laser pulse in the snapshots shown in Figure 2b. The interaction of Shockley partials with each other leads to the formation of immobile stair-rod dislocation segments (Lomer–Cottrell locks), which prevent further propagation of dislocations into the bulk of the crystal as well as their retraction to the crystal–liquid interface. Calculations of the stacking fault energies predicted by the Bonny potential[48] yielded the value that is approximately two times lower for $Ni_{50}Fe_{50}$ than for Ni. The lower value of the stacking fault energy in the alloy agrees with predictions of thermodynamic calculations[66] and can be related to the suppression of the emission of trailing dislocations from the crystal–liquid interface, leading to the retainment of the large area stacking faults connecting the stair-rod dislocations to the melting/solidification front. The partial dislocations and the corresponding stacking faults are extended toward the surface during the solidification process, forming a continuous dislocation network in the resolidified part of the target, Figure 3b.

No dislocations are identified in the resolidified region of the $Ni_{80}Fe_{20}$ target, and only a few small dislocation loops are observed in the $Ni_{80}Cr_{20}$ target. The latter dislocation loops are formed during the resolidification by the same mechanism as the one discussed above for the Ni target. To understand the virtual absence of dislocations in these two alloys, the roughness of the crystal–liquid interface is analyzed. The targets are divided into small $0.4 \times 0.4 \times 0.4$ nm^3 cells each containing 4–6 atoms, and the cells located at the crystal–liquid interface are identified based on the local atomic structure. The standard deviations of the depth of the interfacial cells are calculated for Ni, $Ni_{50}Fe_{50}$, $Ni_{80}Fe_{20}$, and $Ni_{80}Cr_{20}$ targets and are summarized in Table 2. The calculations of the interface roughness are performed for two moments of time during resolidification for each target: 100 and 200 ps for Ni and $Ni_{50}Fe_{50}$, 200 and 300 ps for $Ni_{80}Fe_{20}$,

DOI: 10.1021/acs.jpcc.8b09922
J. Phys. Chem. C 2019, 123, 2202–2215

Table 2. Roughness of the Solidification Front Generated in the Simulations of Laser-Induced Melting and Resolidification of Ni, $Ni_{50}Fe_{50}$, $Ni_{80}Fe_{20}$, and $Ni_{80}Cr_{20}$ Targets Calculated as Standard Deviation of the Local Depth of the Interface Below the Target Surface and Listed in Units of Angstrom[a]

time	Ni	$Ni_{50}Fe_{50}$	$Ni_{80}Fe_{20}$	$Ni_{80}Cr_{20}$
A	23.58	4.01	3.01	3.40
B	13.88	4.81	3.36	3.26

[a]The roughness is evaluated for times marked by stars and labeled as "A" and "B" in Figure 1.

and 300 and 400 ps for $Ni_{80}Cr_{20}$, as marked by stars in the pressure contour plots shown in Figure 1. The results shown in Table 2 reveal that the crystal−liquid interface is much rougher in the Ni target irradiated by a 100 fs laser pulse as compared to the two targets irradiated by longer 50 ps laser pulses, which is consistent with visual analysis of the corresponding snapshots in Figure 2. As mentioned above, high interface roughness is the prerequisite for the formation of dislocations through folding of deep troughs at the interface, and the low values of the interface roughness calculated for $Ni_{80}Fe_{20}$ and $Ni_{80}Cr_{20}$ alloys are consistent with low densities (or absence) of the dislocations in Figure 2c,d. Note that although the interface roughness in $Ni_{80}Cr_{20}$ is similar to that of $Ni_{80}Fe_{20}$, a small number of dislocation loops are generated in the $Ni_{80}Cr_{20}$ target while no dislocations are found in the resolidified $Ni_{80}Fe_{20}$ target. This observation can be explained by the lower stacking fault energy in $Ni_{80}Cr_{20}$,[48,66] which makes it easier for loops of partial dislocations enclosing the stacking faults to form. The interface roughness in the $Ni_{50}Fe_{50}$ target is much lower than that in the pure Ni target because of faster and more localized heating, which leads to a rapid melting of the surface region before the arrival of the unloading tensile wave. In this case, the interaction of the unloading wave with the melting front results in the emission of partial dislocations rather than homogeneous nucleation of liquid-phase regions below the crystal−liquid interface observed for Ni.

Turning to the analysis of vacancies generated by the laser-induced melting and resolidification, the presence of high vacancy concentrations in the resolidified parts of the targets is apparent in the snapshots shown in Figure 2. An even clearer view of the vacancies is provided in Figure 4, where all other

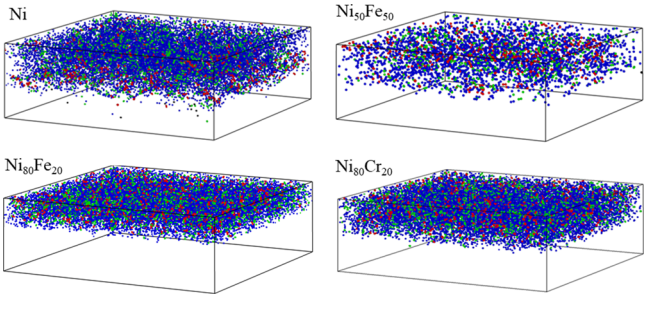

Figure 4. Final snapshots of atomic configurations generated by the end of the resolidification process (340 ps for Ni and $Ni_{50}Fe_{50}$, 500 ps for $Ni_{80}Fe_{20}$ and $Ni_{80}Cr_{20}$), where only the vacancies and vacancy clusters are shown. The atoms surrounding individual vacancies, divacancies, and larger vacancy clusters are colored by blue, green, and red, respectively.

defects are blanked and the single vacancies, divacancies, and larger clusters of vacancies are colored blue, green, and red, respectively. The visual analysis of Figure 4 suggests that while high vacancy concentrations are produced in all four targets, the generation of vacancies is strongly suppressed in $Ni_{50}Fe_{50}$ as compared to other targets. This observation is quantified in Figure 5, where the corresponding spatial distributions of vacancies within the irradiated targets are shown. As compared to Ni, where the vacancy concentration in the resolidified region is ∼0.1%, the vacancy concentration is reduced by a factor of ∼5, down to ∼0.02%, in $Ni_{50}Fe_{50}$. This large suppression of the vacancy generation, however, is not observed in $Ni_{80}Fe_{20}$ and $Ni_{80}Cr_{20}$ alloys, where the vacancy concentrations of about 0.15 and 0.1% are observed, respectively. Analysis of the temperature dependence of the vacancy mobility indicates that it takes more than 10 ns for a vacancy diffusion length to reach 1 nm at a temperature of 0.8 T_m, which is above the temperature of the surface region at the end of the simulations. Given the ultrafast cooling rate, on the order of 10^{12} K/ps at the time of complete resolidification, and the exponential dependence of the mobility of vacancies on temperature, the high concentration of vacancies generated in the surface regions of the targets can be expected to be "frozen in" and remain after cooling down to the ambient temperature.

Another unexpected result related to the vacancy generation in the alloy systems is revealed in the analysis of the local composition in the immediate vicinity of the vacancies. Assuming a random distribution of atoms of different types in the solid−solution alloys, the probability of having k Ni atoms among the 12 atoms constituting the first neighbor shell of a vacancy site is given by the following equation:

$$F_k = \frac{12!}{k!(12-k)!} \cdot p^k \cdot (1-p)^{12-k} \quad (1)$$

where p is the probability of a lattice site to be occupied by Ni atom, which is equal to 0.5 for the $Ni_{50}Fe_{50}$ alloy and 0.8 for both $Ni_{80}Fe_{20}$ and $Ni_{80}Cr_{20}$ alloys. The distributions calculated for the atomic configurations generated in the TTM−MD simulations for Ni−Fe alloy targets and shown in the form of the histograms in Figure 6a,b exhibit a pronounced shift toward lower number of Ni atoms with respect to the random distribution of different types of atoms given by eq 1. The peaks of the histograms shown in Figure 6a,b are shifted from 6 to 5 and from 10 to 9 Ni atoms, respectively, indicating the preference for vacancies to be surrounded by Fe atoms. The frequency histogram calculated for Ni atoms within the first vacancy neighbor shell for $Ni_{80}Cr_{20}$ alloy, Figure 6c, however, coincides with the distribution given by eq 1.

In all targets, the high vacancy concentration is only observed in the regions that experienced transient melting and resolidification, see Figure 5. Therefore, to explain the high vacancy concentrations exceeding the equilibrium values at the melting temperature by about an order of magnitude, the unexpected sensitivity of the generation of vacancies to the target composition, and the deviation from the chemical disorder around the individual vacancies we perform an additional series of simulations of solidification under conditions of fixed undercooling below the equilibrium melting temperature. The results of these simulations are reported below in Section 4.

DOI: 10.1021/acs.jpcc.8b09922
J. Phys. Chem. C 2019, 123, 2202−2215

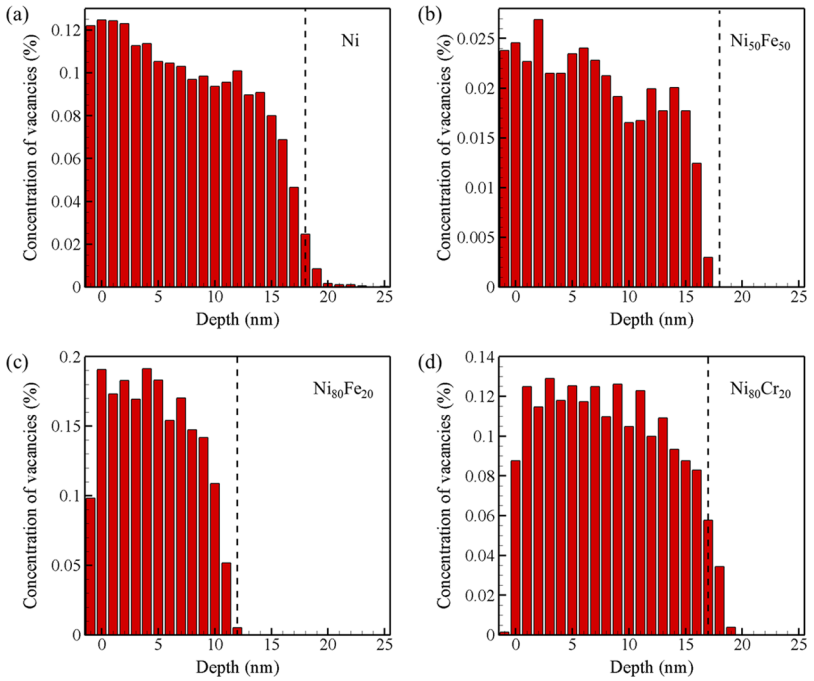

Figure 5. Distribution of vacancy concentration with respect to the depth under irradiated surface for Ni (a), $Ni_{50}Fe_{50}$ (b), $Ni_{80}Fe_{20}$ (c), and $Ni_{80}Cr_{20}$ (d) targets. The dashed lines mark the maximum melting depth reached after the laser irradiation. The vacancy concentrations account for single vacancies and divacancies (counted as two vacancies), but not larger vacancy clusters.

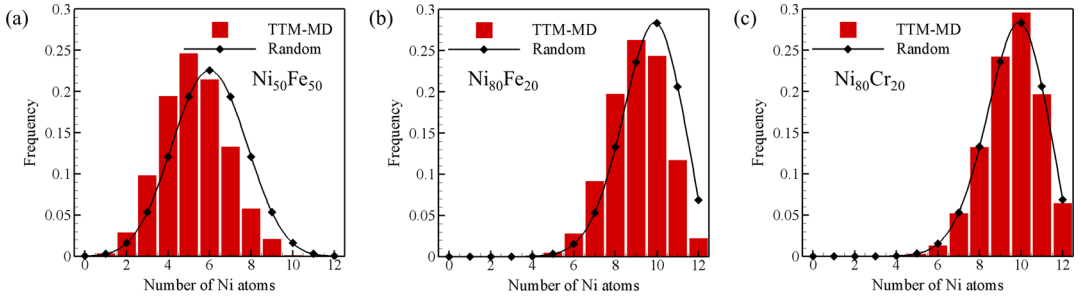

Figure 6. Distribution of the number of Ni atoms in the first nearest neighbor shell of individual vacancies generated by the end of the solidification process in the TTM−MD simulations of laser irradiation of $Ni_{50}Fe_{50}$ (a), $Ni_{80}Fe_{20}$ (b), and $Ni_{80}Cr_{20}$ (c) alloys. The black lines show the distributions expected for a random arrangement of atoms and given by eq 1.

4. ATOMISTIC SIMULATIONS OF VACANCY FORMATION AT A FIXED LEVEL OF UNDERCOOLING

The physical interpretation of the high levels of vacancy supersaturation produced by the laser-induced melting and resolidification as well as the suppression of vacancy generation in $Ni_{50}Fe_{50}$ alloy can be assisted by considering the results of MD simulations of solidification occurring at fixed levels of undercooling below the equilibrium melting temperature. The computational setup used in these simulations is described in Section 2 and schematically illustrated in Figure 7a. A crystalline seed with two (001) crystal−liquid interfaces grows epitaxially under conditions of zero pressure and a controlled level of undercooling.

The steady-state propagation of the two solidification fronts proceeds with a constant velocity defined by the temperature maintained throughout the system, as illustrated by the contour plots depicting the local fraction of the liquid phase, Figure 7b−d. The local fraction of liquid phase, F_{liq}, is determined based on calculation of local order parameter[41,67] that identifies atoms with local surroundings characteristic of liquid or crystalline phases. When the undercooling approaches a critical level of ∼30% below T_m, the homogeneous nucleation of new crystallites inside the strongly undercooled liquid is observed in addition to the epitaxial propagation of the solidification fronts, as exemplified by the emergence of a new region with nonzero fraction of crystalline atoms inside the liquid phase region in a simulation performed at 0.71 T_m, Figure 7d. The onset of homogeneous nucleation of new crystallites has been observed at similar levels of undercooling in earlier simulations of laser melting and resolidification performed for Foiles−Baskes−Daw EAM Ag,[11−13] and at a deeper undercooling of ∼0.60 T_m for Johnson EAM Ni.[8] To avoid the effect of the homogeneous nucleation of new crystallites on the analysis of the vacancy formation at the solidification front, only the results obtained at temperatures ranging from 0.98−0.99 T_m down to the threshold for the onset of the homogenous nucleation are used in the analysis. Two representative atomic configurations showing the presence of vacancies, divacancies, and vacancy clusters in the solidified region of Ni and $Ni_{50}Fe_{50}$ systems are provided in

DOI: 10.1021/acs.jpcc.8b09922
J. Phys. Chem. C 2019, 123, 2202−2215

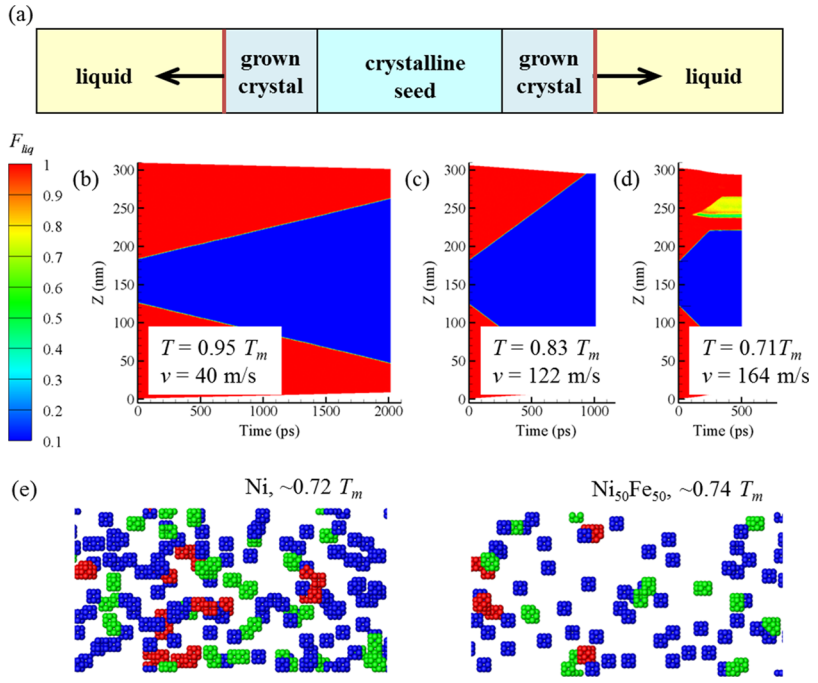

Figure 7. Analysis of the generation of vacancies in MD simulations of the solidification front propagation. (a) Schematic illustration of the computational setup used for simulation of solidification under conditions of constant temperature and zero pressure. (b–d) Contour plots depicting the evolution of the fraction of liquid phase in MD simulations performed for the $Ni_{50}Fe_{50}$ system at temperatures of 0.95 T_m, 0.83 T_m, and 0.71 T_m, respectively. The values of the solidification front velocities calculated from the rates of advancement of the crystal regions (blue) into the molten parts of the system (red) are provided on the plots. (e) Parts of the solidified regions produced in simulations of Ni and $Ni_{50}Fe_{50}$ systems. The atoms surrounding individual vacancies, divacancies, and vacancy clusters are colored by blue, green, and red colors, respectively.

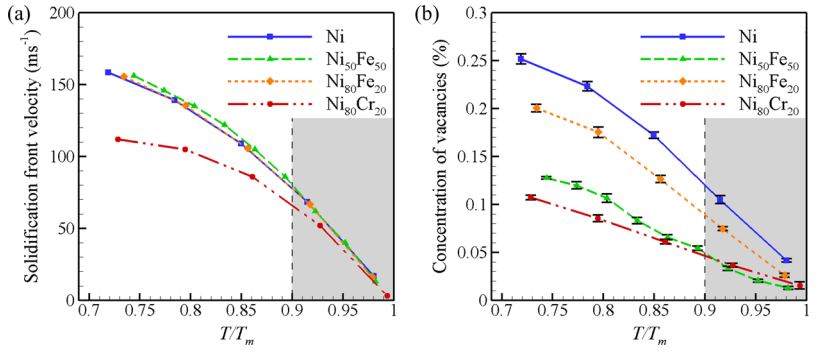

Figure 8. Temperature dependence of solidification velocity (a) and concentration of vacancies (b) generated in MD simulations of solidification of Ni, $Ni_{50}Fe_{50}$, $Ni_{80}Fe_{20}$, and $Ni_{80}Cr_{20}$ performed under conditions of zero pressure and fixed undercooling below the equilibrium melting temperature. The gray zone indicates the range of temperatures observed in TTM–MD simulations of laser-induced melting and resolidification discussed in Section 3.

Figure 7e. The vacancies are counted, and the vacancy concentrations are calculated for the atomic configurations generated at different levels of undercooling.

The solidification velocities and the average concentrations of vacancies in the solidified parts of the four systems, predicted in the simulations, are plotted as functions of temperature in Figure 8. The solidification front velocities are similar in Ni, $Ni_{50}Fe_{50}$, and $Ni_{80}Fe_{20}$, while a reduced velocity is observed for the $Ni_{80}Cr_{20}$ alloy, Figure 8a. At the maximum undercooling achieved by the end of the solidification process in TTM–MD simulations of laser-induced melting and resolidification, 0.9 T_m, the solidification velocity is ~80 m/s for Ni and Ni–Fe systems and ~70 m/s for $Ni_{80}Cr_{20}$ alloy, which agrees with the maximum velocities of the resolidification front in the TTM–MD simulations (see Section 3.2).

The comparison of Figures 8a and 8b reveals similarity of the temperature dependences of the solidification front velocity and vacancy concentration, both exhibiting increase with decreasing temperature. The acceleration of the solidification velocity with increased undercooling can be attributed to the rapid increase in the thermodynamic driving force for crystallization. Indeed, close to linear increase of the solidification front velocities up to a maximum level ~100 m/s followed by a saturation with increasing undercooling has been reported in earlier MD simulations[68] and supported by experimental measurements.[19] The increase in the vacancy concentration, however, looks surprising from the first sight, as the thermodynamic driving force for the generation of vacancies is decreasing exponentially with decreasing temperature. The generation of vacancies, therefore, can only be

DOI: 10.1021/acs.jpcc.8b09922
J. Phys. Chem. C 2019, 123, 2202–2215

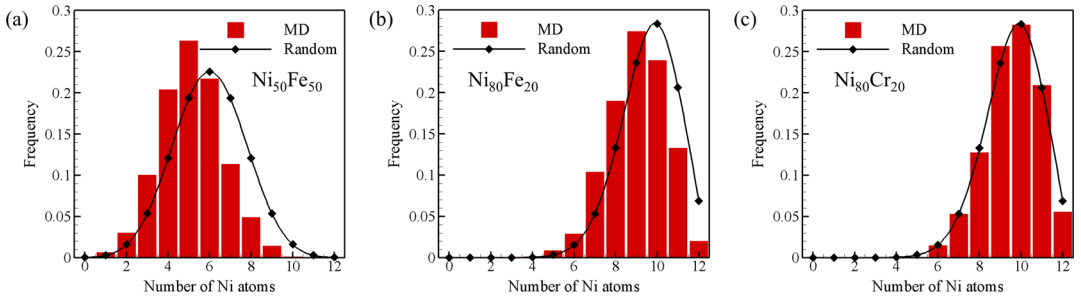

Figure 9. Distribution of the number of Ni atoms in the first nearest neighbor shell of individual vacancies generated in MD simulations of solidification process proceeding at 0.74 T_m and zero pressure in $Ni_{50}Fe_{50}$ (a), $Ni_{80}Fe_{20}$ (b), and $Ni_{80}Cr_{20}$ (c) systems. The black lines show the distributions expected for a random arrangement of atoms and given by eq 1.

explained by peculiarities of the kinetics of the increasingly rapid growth of the crystal at lower temperatures: the vacancies are essentially generated as "errors" in the process of building the crystal structure at the solidification front rapidly advancing under conditions of strong undercooling below the equilibrium melting temperature of the material. The increase of the interface velocity with increasing undercooling, Figure 8a, reduces the time available for atomic rearrangements needed to correct these "errors." Moreover, the mobility of vacancies decreases exponentially with temperature decrease, thus preventing the vacancies from escaping to the liquid phase.

While the vacancy concentrations predicted for different material systems exhibit qualitatively similar dependencies on the level of undercooling, Figure 8b, the plots also demonstrate an obvious suppression of the vacancy generation in the three alloy systems with respect to pure Ni. At all levels of undercooling, the vacancy concentration decreases with addition of Fe, from pure Ni to $Ni_{80}Fe_{20}$ and to $Ni_{50}Fe_{50}$. The addition of Cr has even stronger effect on the vacancy concentration, with $Ni_{80}Cr_{20}$ exhibiting the lowest vacancy concentrations out of the four systems below 0.9 T_m. The suppression of vacancy generation in the solid−solution alloys can be related to a combined effect of the higher energy of the vacancy formation in $Ni_{50}Fe_{50}$, $Ni_{80}Fe_{20}$, and $Ni_{80}Cr_{20}$ as compared to pure Ni[40] and the enhanced mobility of the vacancies in the alloy systems.[69] The higher energy of vacancy formation may reduce the number of vacancies that can be generated at the solidification front, while the higher mobility facilitates their escape into the liquid phase.[70]

The reduced concentrations of vacancies in the alloy systems are consistent with the results of TTM−MD simulations for Ni and $Ni_{50}Fe_{50}$, where levels of the vacancy concentration in the resolidified regions, Figure 5a,b, are close to the ones obtained in the constant temperature and pressure simulations, Figure 8b. The suppression of vacancy generation, however, is not observed in the laser irradiated $Ni_{80}Fe_{20}$ and $Ni_{80}Cr_{20}$ targets, Figure 5c,d, where the average vacancy concentration in the resolidified regions is 1.5−2 times higher than the levels one would expect based on the results of the constant temperature simulations. Moreover, the vacancy concentration in the laser-irradiated $Ni_{80}Fe_{20}$, Figure 5c, is the highest of the four targets and exceeds that in the pure Ni target. This apparent contradiction can be explained by the presence of substantial residual compressive stresses in the resolidified regions of $Ni_{80}Fe_{20}$ and $Ni_{80}Cr_{20}$ targets, which can be seen in the pressure contour plots shown in Figure 1c,d. These thermo-elastic stresses cannot relax through uniaxial expansion of the target in the direction normal to the target and will remain in the surface region until it cools down to the ambient temperature. Meanwhile, as discussed in Section 3, in Ni and $Ni_{50}Fe_{50}$ targets the residual stresses are relaxed by the generation of dislocations and, as a result, the vacancy concentrations in the resolidified regions are in accord with the predictions of zero pressure simulations performed at comparable levels of undercooling.

Finally, the deviation from the chemical disorder around the individual vacancies observed for the Ni−Fe alloy targets in the TTM−MD simulations, Figure 6a,b, is confirmed in the MD simulations of solidification occurring under conditions of fixed undercooling. The analysis of the first atomic shells surrounding the vacancy sites in the alloy systems reveals the preference for vacancy sites to be surrounded by Fe atoms in the $Ni_{50}Fe_{50}$ and $Ni_{80}Fe_{20}$ systems, as reflected in the pronounced shift of the distributions calculated in MD simulations to the left with respect to the binomial distributions given by eq 1, Figure 9a,b. The appearance of atomic-scale chemical heterogeneities in the immediate vicinity of the vacancy sites is also apparent from the average numbers of Ni atoms present in the first neighbor shells of the vacancies listed in Table 3. The number of Ni atoms is substantially reduced with respect to the values that correspond to the random mixing in the alloy systems, 6 Ni neighbors for 50 at.% Ni and 9.6 Ni neighbors for 80 at.% Ni alloys. A detailed computational analysis has revealed that the average vacancy formation energy increases with increasing number of Ni atoms in the first neighbor shell of a vacancy site. Thus, while the vacancies have random chemical environment immediately after their incorporation into the rapidly growing crystal, the following atomic jumps shift the vacancy environment toward the energetically favorable configurations with Fe-rich first

Table 3. Average Number of Ni Atoms in the First Neighbor Shells of Individual Vacancies Expected for a Random Arrangement of Atoms of Different Types in the Alloys, Predicted in the TTM−MD Simulations of Laser-Induced Melting and Resolidification, and Calculated in MD Simulations of Solidification Performed at a Fixed Temperature of 0.74 T_m[a]

	$Ni_{50}Fe_{50}$	$Ni_{80}Fe_{20}$	$Ni_{80}Cr_{20}$
random	6.00	9.60	9.60
TTM−MD	5.25	9.06	9.59
MD	5.13	9.04	9.59

[a]The corresponding distributions of the number of Ni atoms in the first neighbor shells around the vacancy sites are shown in Figures 6 and 9 for the TTM−MD and MD simulations, respectively.

DOI: 10.1021/acs.jpcc.8b09922
J. Phys. Chem. C 2019, 123, 2202−2215

neighbor shells. The positive relationship between the vacancy formation energy and the number of Ni first shell neighbors of the vacancy site is not observed in the $Ni_{80}Cr_{20}$ alloy, and the vacancy configurations do not exhibit any noticeable deviation from the random mixing of the two components of the alloy, Figure 9c and Table 3. This observation is consistent with the results of the TTM−MD simulation of melting and resolidification of a Ni−Cr alloy target discussed in Section 3, Figure 6c.

5. CONCLUSIONS

The short-pulse laser induced generation of crystal defects, including vacancies, dislocation, stacking faults, and twin boundaries, in Ni and Ni-based binary solid−solution alloys is investigated in large-scale TTM−MD simulations performed in the irradiation regime of melting and resolidification. The intrinsic chemical disorder in the single-phase concentrated solid−solution alloys reduces the thermal conductivity and strengthens electron−phonon coupling with respect to pure Ni, leading to faster and more localized heating of the surface regions of the irradiated targets. As a result, the laser fluence thresholds for melting and spallation are significantly reduced, the magnitude of the laser-induced stresses increases, and the separation between the two thresholds shrinks in the alloy targets.

The microstructure of the resolidified surface regions in Ni and $Ni_{50}Fe_{50}$ targets irradiated by 100 fs laser pulses is found to be strongly affected by the dynamic relaxation of the laser-induced stresses, which leads to the generation of a strong unloading tensile wave that interacts with the melting front and facilitates the formation high densities of partial dislocations in the surface regions of the irradiated targets. In Ni, the tensile wave passes through the melting front, reduces the crystal stability against melting, and triggers homogenous nucleation of new liquid regions in the superheated crystal. As a result, the crystal−liquid interface formed by the end of the melting process has a rough shape, and the resolidification proceeding from such interface yields a high density of dislocations connected to the solidification front and extending toward the surface in the course of the solidification.

In $Ni_{50}Fe_{50}$ target, numerous Shockley partial dislocations are directly emitted from the crystal−liquid interface at the end of the melting process, when a strong unloading wave passes through the interface. The interaction of Shockley partials with each other leads to the formation of immobile stair-rod dislocation segments, which prevent the retraction of the dislocations to the crystal−liquid interface. The partial dislocations and the corresponding stacking faults are extended toward the surface during the solidification process, forming a continuous dislocation network in the resolidified part of the target.

In $Ni_{80}Fe_{20}$ and $Ni_{80}Cr_{20}$ targets irradiated by longer 50 ps laser pulses, the laser-induced thermoelastic stresses are much lower, and neither the melting front roughening nor dislocation emission is observed in the simulations. As a result, the solidification proceeds through the propagation of a smooth crystal−liquid interface, which yields no dislocations in $Ni_{80}Fe_{20}$ and only a small number of dislocation loops in $Ni_{80}Cr_{20}$. The levels of undercooling at the solidification front are similar to the values reached in the Ni and $Ni_{50}Fe_{50}$ targets irradiated by 100 fs laser pulses. The difference in the microstructure, therefore, is mainly related to the differences in laser-induced stresses and material properties.

One prominent feature of the microstructure formed in the surface regions of the irradiated targets is the generation of very high vacancy concentrations exceeding the equilibrium values at the melting temperature by about an order of magnitude. On the basis of the results of MD simulations of solidification occurring at fixed levels of undercooling and in the absence of mechanical stresses, the generation of vacancies is correlated with the temperature dependence of the velocity of the solidification front. The vacancies are generated as "errors" in the process of building the crystal structure at the solidification front, and the sharp drop in mobility of the vacancies and the increase in the solidification front velocity with increasing undercooling diminish the chances for the vacancies to escape to the liquid phase. As a result, the vacancy concentration generated at the solidification front exhibits a strong increase with increasing undercooling in both pure Ni and Ni-based alloys.

Despite the qualitatively similar dependences on the levels of undercooling, the vacancy generation in the three alloy systems are found to be strongly suppressed with respect to pure Ni. The suppression is observed in all MD simulations performed at different levels of undercooling as well as in the TTM−MD simulation of laser-induced melting and resolidification of the $Ni_{50}Fe_{50}$ target. The suppression of the vacancy generation in the solid−solution alloys is related to combined effect of the enhanced mobility of the vacancies and the higher energy of the vacancy formation in the alloy systems. In $Ni_{80}Fe_{20}$ and $Ni_{80}Cr_{20}$ targets irradiated by 50 ps laser pulses, the vacancy suppression effect is counteracted by the fostered vacancy generation under the action of residual compressive stresses.

The analysis of the first atomic shells surrounding the vacancy sites in Ni−Fe alloys reveals the preference for the vacancy sites to be surrounded by Fe atoms (even though addition of Fe significantly decreases the total vacancy concentration as compared to pure Ni). This observation is an example of how the crystal defects can produce atomic-scale chemical heterogeneities in the single-phase concentrated solid−solution alloys.

Overall, the combination of the TTM−MD simulations of laser-induced melting and resolidification with MD modeling of solidification occurring under well-controlled temperature and pressure conditions has provided important insights into the mechanisms of the generation of crystal defects in Ni-based solid−solution alloys under conditions of strong thermal and mechanical nonequilibrium induced by a rapid energy deposition.

■ ASSOCIATED CONTENT

Supporting Information

The Supporting Information is available free of charge on the ACS Publications website at DOI: 10.1021/acs.jpcc.8b09922.

(1) Electron heat capacity, electron−phonon coupling factor, and thermal conductivity of Ni, $Ni_{50}Fe_{50}$, $Ni_{80}Fe_{20}$, and $Ni_{80}Cr_{20}$ used in the TTM equation for electron temperature; (2) high-temperature thermophysical properties (melting and critical temperatures, surface tension, and lattice heat capacity) of Ni, $Ni_{50}Fe_{50}$, $Ni_{80}Fe_{20}$, and $Ni_{80}Cr_{20}$ predicted by the Bonny EAM potential (PDF)

DOI: 10.1021/acs.jpcc.8b09922
J. Phys. Chem. C 2019, 123, 2202−2215

AUTHOR INFORMATION

Corresponding Author

*E-mail: lz2n@virginia.edu.

ORCID

Leonid V. Zhigilei: 0000-0002-1549-7086

Notes

The authors declare no competing financial interest.

ACKNOWLEDGMENTS

Financial support for this work was provided by the Energy Dissipation to Defect Evolution (EDDE), an Energy Frontier Research Center funded by the U.S. Department of Energy, Office of Science, Basic Energy Sciences under contract number DE-AC05-00OR22725. Computational support was provided by the Oak Ridge Leadership Computing Facility (INCITE project MAT130), National Science Foundation through the Extreme Science and Engineering Discovery Environment (project TG-DMR110090), and the University of Virginia Advanced Research Computing Services.

REFERENCES

(1) Oboňa, J. V.; Ocelík, V.; Rao, J. C.; Skolski, J. Z. P.; Römer, G. R. B. E.; Huis in 't Veld, A. J.; De Hosson, J. T. M. Modification of Cu surface with picosecond laser pulses. *Appl. Surf. Sci.* **2014**, *303*, 118−124.

(2) Kumar, A.; Pollock, T. M. Mapping of femtosecond laser-induced collateral damage by electron backscatter diffraction. *J. Appl. Phys.* **2011**, *110*, 083114.

(3) Sedao, X.; Maurice, C.; Garrelie, F.; Colombier, J.-P.; Reynaud, S.; Quey, R.; Blanc, G.; Pigeon, F. Electron backscatter diffraction characterization of laser-induced periodic surface structures on nickel surface. *Appl. Surf. Sci.* **2014**, *302*, 114−117.

(4) Sedao, X.; Maurice, C.; Garrelie, F.; Colombier, J.-P.; Reynaud, S.; Quey, R.; Pigeon, F. Influence of crystal orientation on the formation of femtosecond laser-induced periodic surface structures and lattice defects accumulation. *Appl. Phys. Lett.* **2014**, *104*, 171605.

(5) Titus, M. S.; Echlin, M. P.; Gumbsch, P.; Pollock, T. M. Dislocation injection in strontium titanate by femtosecond laser pulses. *J. Appl. Phys.* **2015**, *118*, 075901.

(6) Echlin, M. P.; Titus, M. S.; Straw, M.; Gumbsch, P.; Pollock, T. M. Materials response to glancing incidence femtosecond laser ablation. *Acta Mater.* **2017**, *124*, 37−46.

(7) Sedao, X.; Shugaev, M. V.; Wu, C.; Douillard, T.; Esnouf, C.; Maurice, C.; Reynaud, S.; Pigeon, F.; Garrelie, F.; Zhigilei, L. V.; et al. Growth twinning and generation of high-frequency surface nanostructures in ultrafast laser-induced transient melting and resolidification. *ACS Nano* **2016**, *10*, 6995−7007.

(8) Ivanov, D. S.; Lin, Z.; Rethfeld, B.; O'Connor, G. M.; Glynn, T. J.; Zhigilei, L. V. Nanocrystalline structure of nanobump generated by localized photoexcitation of metal film. *J. Appl. Phys.* **2010**, *107*, 013519.

(9) Lin, Z.; Johnson, R. A.; Zhigilei, L. V. Computational study of the generation of crystal defects in a bcc metal target irradiated by short laser pulses. *Phys. Rev. B: Condens. Matter Mater. Phys.* **2008**, *77*, 214108.

(10) Wu, C.; Thomas, D. A.; Lin, Z.; Zhigilei, L. V. Runaway lattice-mismatched interface in an atomistic simulation of femtosecond laser irradiation of Ag film-Cu substrate system. *Appl. Phys. A* **2011**, *104*, 781−792.

(11) Wu, C.; Christensen, M. S.; Savolainen, J.-M.; Balling, P.; Zhigilei, L. V. Generation of subsurface voids and a nanocrystalline surface layer in femtosecond laser irradiation of a single-crystal Ag target. *Phys. Rev. B: Condens. Matter Mater. Phys.* **2015**, *91*, 035413.

(12) Wu, C.; Zhigilei, L. V. Nanocrystalline and polyicosahedral structure of a nanospike generated on metal surface irradiated by a single femtosecond laser pulse. *J. Phys. Chem. C* **2016**, *120*, 4438−4447.

(13) Shugaev, M. V.; Shih, C.-Y.; Karim, E. T.; Wu, C.; Zhigilei, L. V. Generation of nanocrystalline surface layer in short pulse laser processing of metal targets under conditions of spatial confinement by solid or liquid overlayer. *Appl. Surf. Sci.* **2017**, *417*, 54−63.

(14) Shugaev, M. V.; Gnilitskyi, I.; Bulgakova, N. M.; Zhigilei, L. V. Mechanism of single-pulse ablative generation of laser-induced periodic surface structures. *Phys. Rev. B* **2017**, *96*, 205429.

(15) Duff, W. H.; Zhigilei, L. V. Computational study of cooling rates and recrystallization kinetics in short pulse laser quenching of metal targets. *J. Phys.: Conf. Ser.* **2007**, *59*, 413−417.

(16) Zhigilei, L. V.; Lin, Z.; Ivanov, D. S. Atomistic modeling of short pulse laser ablation of metals: Connections between melting, spallation, and phase explosion. *J. Phys. Chem. C* **2009**, *113*, 11892−11906.

(17) Lin, C.-J.; Spaepen, F.; Turnbull, D. Picosecond pulsed laser-induced melting and glass formation in metals. *J. Non-Cryst. Solids* **1984**, *61*−*62*, 767−772.

(18) Lin, C.-J.; Spaepen, F. Nickel-niobium alloys obtained by picosecond pulsed laser quenching. *Acta Metall.* **1986**, *34*, 1367−1375.

(19) Chan, W.-L.; Averback, R. S.; Cahill, D. G.; Ashkenazy, Y. Solidification velocities in deeply undercooled silver. *Phys. Rev. Lett.* **2009**, *102*, 095701.

(20) Wu, C.; Karim, E. T.; Volkov, A. N.; Zhigilei, L. V. Atomic movies of laser-induced structural and phase transformations from molecular dynamics simulations. In *Lasers in Materials Science*; Castillejo, M., Ossi, P. M., Zhigilei, L. V., Eds., Springer Series in Materials Science; Springer International Publishing: Switzerland, 2014; Vol. *191*, pp 67−100.

(21) Karim, E. T.; Wu, C.; Zhigilei, L. V. Molecular dynamics simulations of laser-materials interactions: General and material-specific mechanisms of material removal and generation of crystal defects. In *Fundamentals of Laser-Assisted Micro- and Nanotechnologies*; Veiko, V. P., Konov, V. I., Eds., Springer Series in Materials Science; Springer International Publishing: Switzerland, 2014; Vol. *195*, pp 27−49.

(22) Jee, Y.; Becker, M. F.; Walser, R. M. Laser-induced damage on single-crystal metal surfaces. *J. Opt. Soc. Am. B* **1988**, *5*, 648−659.

(23) Mannion, P. T.; Magee, J.; Coyne, E.; O'Connor, G. M.; Glynn, T. J. The effect of damage accumulation behaviour on ablation thresholds and damage morphology in ultrafast laser micro-machining of common metals in air. *Appl. Surf. Sci.* **2004**, *233*, 275−287.

(24) Kirkwood, S. E.; van Popta, A. C.; Tsui, Y. Y.; Fedosejevs, R. Single and multiple shot near-infrared femtosecond laser pulse ablation thresholds of copper. *Appl. Phys. A* **2005**, *81*, 729−735.

(25) Raciukaitis, G.; Brikas, M.; Gecys, P.; Gedvilas, M. Accumulation effects in laser ablation of metals with high-repetition-rate lasers. *Proc. SPIE* **2008**, *7005*, 70052L.

(26) Lasemi, N.; Pacher, U.; Zhigilei, L. V.; Bomatí-Miguel, O.; Lahoz, R.; Kautek, W. Pulsed laser ablation and incubation of nickel, iron and tungsten in liquids and air. *Appl. Surf. Sci.* **2018**, *433*, 772−779.

(27) Armbruster, O.; Naghilou, A.; Kitzler, M.; Kautek, W. Spot size and pulse number dependence of femtosecond laser ablation thresholds of silicon and stainless steel. *Appl. Surf. Sci.* **2017**, *396*, 1736−1740.

(28) Siwick, B. J.; Dwyer, J. R.; Jordan, R. E.; Miller, R. J. D. An atomic-level view of melting using femtosecond electron diffraction. *Science* **2003**, *302*, 1382−1385.

(29) Ernstorfer, R.; Harb, M.; Hebeisen, C. T.; Sciaini, G.; Dartigalongue, T.; Miller, R. J. D. The formation of warm dense matter: Experimental evidence for electronic bond hardening in gold. *Science* **2009**, *323*, 1033−1037.

(30) Chen, J.; Chen, W.-K.; Tang, J.; Rentzepis, P. M. Time-resolved structural dynamics of thin metal films heated with femtosecond optical pulses. *Proc. Natl. Acad. Sci. USA* **2011**, *108*, 18887−18892.

DOI: 10.1021/acs.jpcc.8b09922
J. Phys. Chem. C 2019, 123, 2202−2215

(31) Schäfer, S.; Liang, W.; Zewail, A. H. Structural dynamics of nanoscale gold by ultrafast electron crystallography. *Chem. Phys. Lett.* **2011**, *515*, 278−282.
(32) Bordeaux, N.; Montes-Arango, A. M.; Liu, J.; Barmak, K.; Lewis, L. H. Thermodynamic and kinetic parameters of the chemical order-disorder transformation in $L1_0$ FeNi (tetrataenite). *Acta Mater.* **2016**, *103*, 608−615.
(33) Liu, J.; Riddiford, L. J.; Floristean, C.; Goncalves-Neto, F.; Rezaeeyazdi, M.; Lewis, L. H.; Barmak, K. Kinetics of order-disorder transformation of $L1_2$ $FeNi_3$ in the Fe-Ni system. *J. Alloys Compd.* **2016**, *689*, 593−598.
(34) Wu, Z.; Bei, H.; Pharr, G. M.; George, E. P. Temperature dependence of the mechanical properties of equiatomic solid solution alloys with face-centered cubic crystal structures. *Acta Mater.* **2014**, *81*, 428−441.
(35) Zhang, Y.; Stocks, G. M.; Jin, K.; Lu, C.; Bei, H.; Sales, B. C.; Wang, L.; Béland, L. K.; Stoller, R. E.; Samolyuk, G. D.; et al. Influence of chemical disorder on energy dissipation and defect evolution in concentrated solid-solution alloys. *Nat. Commun.* **2015**, *6*, 8736.
(36) Jin, K.; Sales, B. C.; Stocks, G. M.; Samolyuk, G. D.; Daene, M.; Weber, W. J.; Zhang, Y.; Bei, H. Tailoring the physical properties of Ni-based single-phase equiatomic alloys by modifying the chemical complexity. *Sci. Rep.* **2016**, *6*, 20159.
(37) Granberg, F.; Nordlund, K.; Ullah, M. W.; Jin, K.; Lu, C.; Bei, H.; Wang, L. M.; Djurabekova, F.; Weber, W. J.; Zhang, Y. Mechanism of radiation damage reduction in equiatomic multicomponent single phase alloys. *Phys. Rev. Lett.* **2016**, *116*, 135504.
(38) Béland, L. K.; Lu, C.; Osetskiy, Y. N.; Samolyuk, G. D.; Caro, A.; Wang, L.; Stoller, R. E. Features of primary damage by high energy displacement cascades in concentrated Ni-based alloys. *J. Appl. Phys.* **2016**, *119*, 085901.
(39) Ullah, M. W.; Aidhy, D. S.; Zhang, Y.; Weber, W. J. Damage accumulation in ion-irradiated Ni-based concentrated solid-solution alloys. *Acta Mater.* **2016**, *109*, 17−22.
(40) Zhao, S.; Stocks, G. M.; Zhang, Y. Defect energetics of concentrated solid-solution alloys from ab initio calculations: $Ni_{0.5}Co_{0.5}$, $Ni_{0.5}Fe_{0.5}$, $Ni_{0.8}Fe_{0.2}$ and $Ni_{0.8}Cr_{0.2}$. *Phys. Chem. Chem. Phys.* **2016**, *18*, 24043−24056.
(41) Ivanov, D. S.; Zhigilei, L. V. Combined atomistic-continuum modeling of short-pulse laser melting and disintegration of metal films. *Phys. Rev. B: Condens. Matter Mater. Phys.* **2003**, *68*, 064114.
(42) Wu, C.; Zhigilei, L. V. Microscopic mechanisms of laser spallation and ablation of metal targets from large-scale molecular dynamics simulations. *Appl. Phys. A* **2014**, *114*, 11−32.
(43) Anisimov, S. I.; Kapeliovich, B. L.; Perel'man, T. L. Electron emission from metal surfaces exposed to ultrashort laser pulses. *Zh. Eksp. Teor. Fiz.* **1974**, *66*, 776−781; *Sov. Phys. JETP* **1974**, *39*, 375−377.
(44) Ivanov, D. S.; Zhigilei, L. V. Combined atomistic-continuum model for simulation of laser interaction with metals: Application in the calculation of melting thresholds in Ni targets of varying thickness. *Appl. Phys. A* **2004**, *79*, 977−981.
(45) Lin, Z.; Zhigilei, L. V.; Celli, V. Electron-phonon coupling and electron heat capacity of metals under conditions of strong electron-phonon nonequilibrium. *Phys. Rev. B: Condens. Matter Mater. Phys.* **2008**, *77*, 075133.
(46) Lin, Z.; Zhigilei, L. V. Temperature dependences of the electron−phonon coupling, electron heat capacity and thermal conductivity in Ni under femtosecond laser irradiation. *Appl. Surf. Sci.* **2007**, *253*, 6295−6300.
(47) Samolyuk, G. D.; Béland, L. K.; Stocks, G. M.; Stoller, R. E. Electron-phonon coupling in Ni-based binary alloys with application to displacement cascade modeling. *J. Phys.: Condens. Matter* **2016**, *28*, 175501.
(48) Bonny, G.; Terentyev, D.; Pasianot, R. C.; Poncé, S.; Bakaev, A. Interatomic potential to study plasticity in stainless steels: The FeNiCr model alloy. *Modelling Simul. Mater. Sci. Eng.* **2011**, *19*, 085008.
(49) Zhigilei, L. V.; Garrison, B. J. Pressure waves in microscopic simulations of laser ablation. *Mater. Res. Soc. Symp. Proc.* **1999**, *538*, 491−496.
(50) Schäfer, C.; Urbassek, H. M.; Zhigilei, L. V.; Garrison, B. J. Pressure-transmitting boundary conditions for molecular-dynamics simulations. *Comp. Mater. Sci.* **2002**, *24*, 421−429.
(51) Palik, E. D. *Handbook of Optical Constants of Solids*; Academic Press: New York, 1998.
(52) Luo, S.-N.; Ahrens, T. J.; Çağın, T.; Strachan, A.; Goddard, W. A., III; Swift, D. C. Maximum superheating and undercooling: Systematics, molecular dynamics simulations, and dynamic experiments. *Phys. Rev. B: Condens. Matter Mater. Phys.* **2003**, *68*, 134206.
(53) Ivanov, D. S.; Zhigilei, L. V. Effect of pressure relaxation on the mechanisms of short-pulse laser melting. *Phys. Rev. Lett.* **2003**, *91*, 105701.
(54) Lin, Z.; Leveugle, E.; Bringa, E. M.; Zhigilei, L. V. Molecular dynamics simulation of laser melting of nanocrystalline Au. *J. Phys. Chem. C* **2010**, *114*, 5686−5699.
(55) Berendsen, H. J. C.; Postma, J. P. M.; van Gunsteren, W. F.; DiNola, A.; Haak, J. R. Molecular dynamics with coupling to an external bath. *J. Chem. Phys.* **1984**, *81*, 3684−3690.
(56) Mishin, Y. Atomistic modeling of the γ and γ'-phases of the Ni-Al system. *Acta Mater.* **2004**, *52*, 1451−1467.
(57) Zhou, X. W.; Wadley, H. N. G.; Johnson, R. A.; Larson, D. J.; Tabat, N.; Cerezo, A.; Petford-Long, A. K.; Smith, G. D. W.; Clifton, P. H.; Martens, R. L.; et al. Atomic scale structure of sputtered metal multilayers. *Acta Mater.* **2001**, *49*, 4005−4015.
(58) Zhigilei, L. V.; Garrison, B. J. Microscopic mechanisms of laser ablation of organic solids in the thermal and stress confinement irradiation regimes. *J. Appl. Phys.* **2000**, *88*, 1281−1298.
(59) Paltauf, G.; Dyer, P. E. Photomechanical processes and effects in ablation. *Chem. Rev.* **2003**, *103*, 487−518.
(60) Ivanov, D. S.; Zhigilei, L. V. Kinetic limit of heterogeneous melting in metals. *Phys. Rev. Lett.* **2007**, *98*, 195701.
(61) Savolainen, J.-M.; Christensen, M. S.; Balling, P. Material swelling as the first step in the ablation of metals by ultrashort laser pulses. *Phys. Rev. B: Condens. Matter Mater. Phys.* **2011**, *84*, 193410.
(62) Ashitkov, S. I.; Inogamov, N. A.; Zhakhovskii, V. V.; Emirov, Y. N.; Agranat, M. B.; Oleinik, I. I.; Anisimov, S. I.; Fortov, V. E. Formation of nanocavities in the surface layer of an aluminum target irradiated by a femtosecond laser pulse. *JETP Lett.* **2012**, *95*, 176−181.
(63) Stukowski, A. Structure identification methods for atomistic simulations of crystalline materials. *Modelling Simul. Mater. Sci. Eng.* **2012**, *20*, 045021.
(64) Stukowski, A.; Bulatov, V. V.; Arsenlis, A. Automated identification and indexing of dislocations in crystal interfaces. *Modelling Simul. Mater. Sci. Eng.* **2012**, *20*, 085007.
(65) Stukowski, A.; Albe, K. Extracting dislocations and non-dislocation crystal defects from atomistic simulation data. *Modelling Simul. Mater. Sci. Eng.* **2010**, *18*, 085001.
(66) Miodownik, A. P. The calculation of stacking fault energies in Fe−Ni−Cr alloys. *CALPHAD: Comput. Coupling Phase Diagrams Thermochem.* **1978**, *2*, 207−226.
(67) Morris, J. R.; Song, X. The melting lines of model systems calculated from coexistence simulations. *J. Chem. Phys.* **2002**, *116*, 9352−9358.
(68) Ashkenazy, Y.; Averback, R. S. Kinetic stages in the crystallization of deeply undercooled body-centered-cubic and face-centered-cubic metals. *Acta Mater.* **2010**, *58*, 524−530.
(69) Zhao, S.; Velisa, G.; Xue, H.; Bei, H.; Weber, W. J.; Zhang, Y. Suppression of vacancy cluster growth in concentrated solid solution alloys. *Acta Mater.* **2017**, *125*, 231−237.
(70) Hillert, M.; Schwind, M.; Selleby, M. Trapping of vacancies by rapid solidification. *Acta Mater.* **2002**, *50*, 3283−3291.

DOI: 10.1021/acs.jpcc.8b09922
J. Phys. Chem. C 2019, 123, 2202−2215